

## Supporting Information

**Title****Atomically Sharp Heterophase Interfaces in Cation-Eutaxy A–III–V Compounds**

*Seungyeon Kim*<sup>1,2,7</sup>, *Jongbum Won*<sup>1,2,7</sup>, *Taeyoung Kim*<sup>1,2,7</sup>, *Hong Choi*<sup>1,2</sup>, *Seokmin Park*<sup>1,2</sup>,  
*Jinwoo Cheon*<sup>3,4,5</sup>, *Jae-Hyun Lee*<sup>4,5</sup>, *Young Jin Choi*<sup>6</sup>, *Wooyoung Shim*<sup>1,2,4,5\*</sup>

<sup>1</sup>Department of Materials Science and Engineering, Yonsei University, Seoul 03722, Korea.

<sup>2</sup>Center for Multi-Dimensional Materials, Yonsei University, Seoul 03722, Korea.

<sup>3</sup>Department of Chemistry, Yonsei University, Seoul 03722, Korea.

<sup>4</sup>Center for Nanomedicine, Institute for Basic Science (IBS), Seoul 03722, Korea

<sup>5</sup>Yonsei IBS Institute, Yonsei University, Seoul 03722, Korea

<sup>6</sup>Department of Nanotechnology and Advanced Materials Engineering, Hybrid Materials Research Center (HMC), Sejong University, Seoul 05006, Korea

<sup>7</sup>These authors contributed equally: Seungyeon Kim, Jongbum Won, Taeyoung Kim

\*Correspondence: wshim@yonsei.ac.kr.

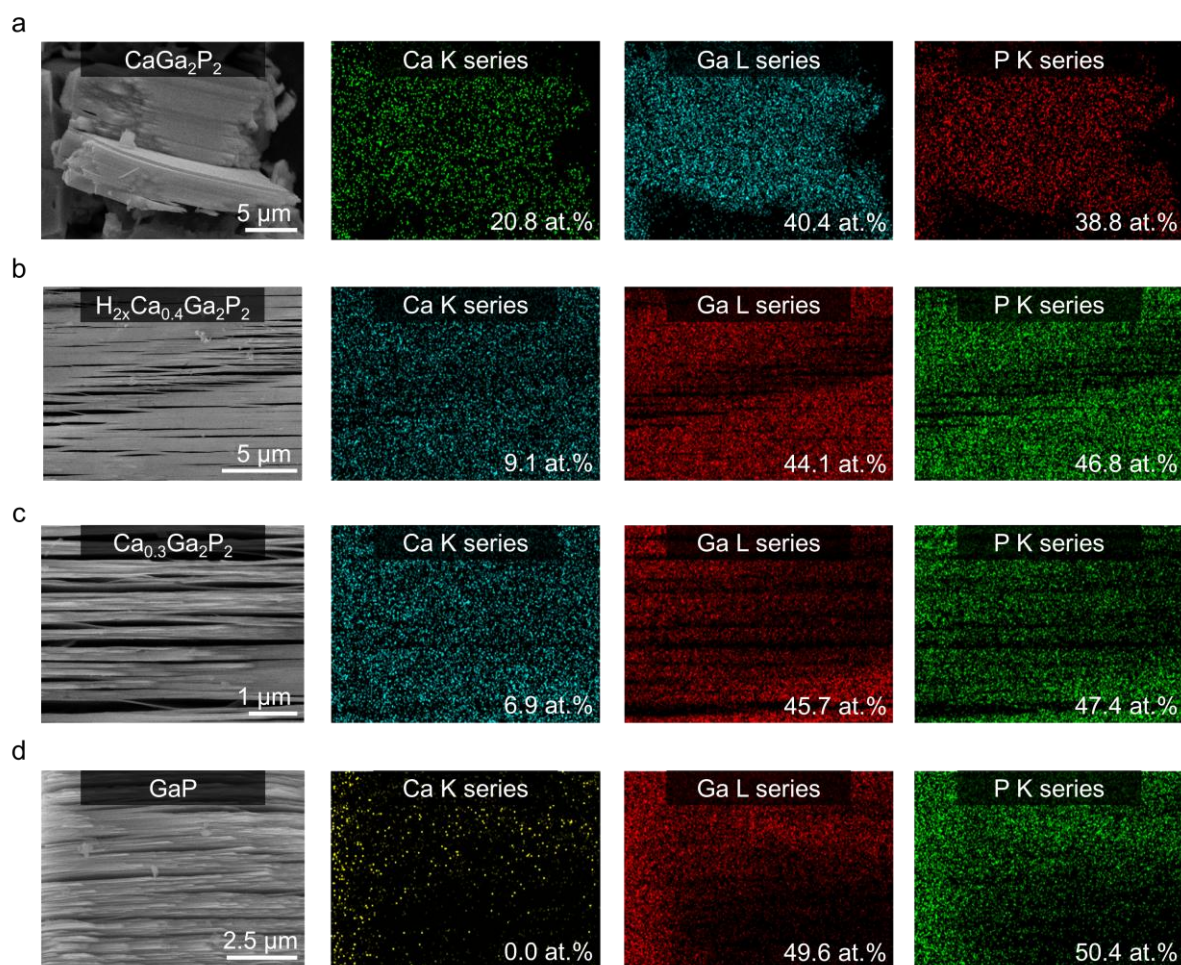
**This PDF file includes:**

Figure S1 to 14

Table S1 to 5

Note S1, 2

Supplementary Methods



**Figure S1.** SEM-EDS elemental mapping of  $\text{CaGa}_2\text{P}_2$ -derived samples with different Ca compositions. (a) Pristine  $\text{CaGa}_2\text{P}_2$ . Layered morphology with uniform Ca/Ga/P distribution (Ca 20.8 at.%, Ga 40.4 at.%, P 38.8 at.%). (b)  $\text{H}_{2x}\text{Ca}_{0.4}\text{Ga}_2\text{P}_2$ . Preserved lamellar structure; reduced Ca signal consistent with partial deintercalation (Ca 9.1 at.%, Ga 44.1 at.%, P 46.8 at.%). (c)  $\text{Ca}_{0.3}\text{Ga}_2\text{P}_2$ . Further Ca depletion reflected in weak Ca signal while Ga and P remain uniformly distributed (Ca 6.9 at.%, Ga 45.7 at.%, P 47.4 at.%). (d)  $\text{GaP}$  (Ca  $\approx$  0). Fully transformed product with no detectable Ca and uniform Ga/P signals (Ga 49.6 at.%, P 50.4 at.%).

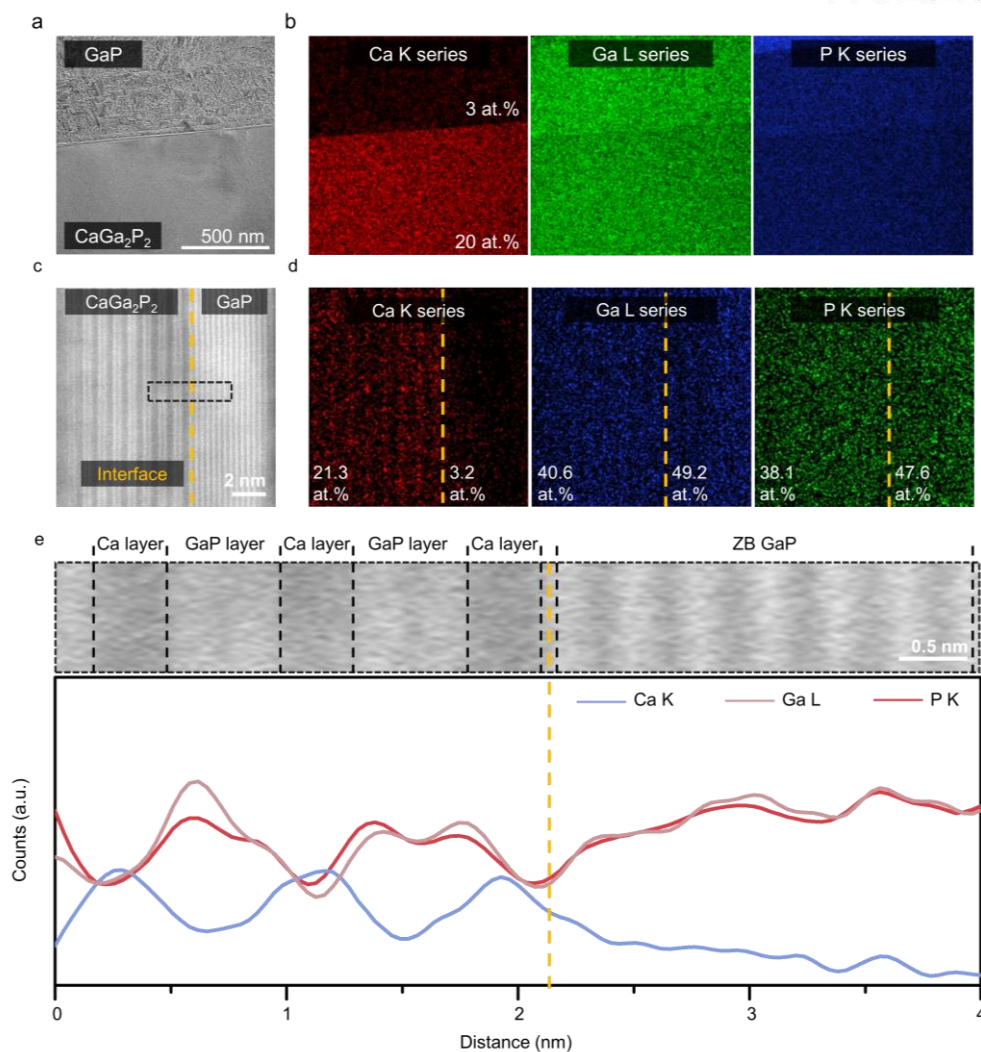


**Figure S2.** TEM–EDS mapping and high-resolution TEM–EDS line-scan of CaGa<sub>2</sub>P<sub>2</sub>/ZB GaP heterophase showing compositionally sharp separation and an abrupt compositional discontinuity. (a,b) TEM (a) and corresponding EDS elemental maps (b) revealing distinct Ca-rich and Ca-poor domains within the heterophase region. The upper domain exhibits Ca  $\approx$  3 at.%, whereas the lower domain shows Ca  $\approx$  20 at.%, while Ga and P remain uniformly distributed across both regions. (c,d) High-resolution TEM image (c) and corresponding EDS elemental maps (d) across the interface, revealing clearly separated Ca-rich and Ca-poor domains. The left region (CaGa<sub>2</sub>P<sub>2</sub>) shows Ca 21.3 at.%, Ga 40.6 at.%, and P 38.1 at.%, whereas the right region (ZB GaP) shows Ca 3.2 at.%, Ga 49.2 at.%, and P 47.6 at.%. (e) Magnified image of the interface (top) and the corresponding EDS line-scan profile (bottom) across the boundary, showing a sharp decrease in the Ca signal at the interface. The abrupt change in Ca concentration indicates a compositionally sharp boundary consistent with an abrupt phase transition at the atomic scale. The black box marks the region corresponding to the magnified image.

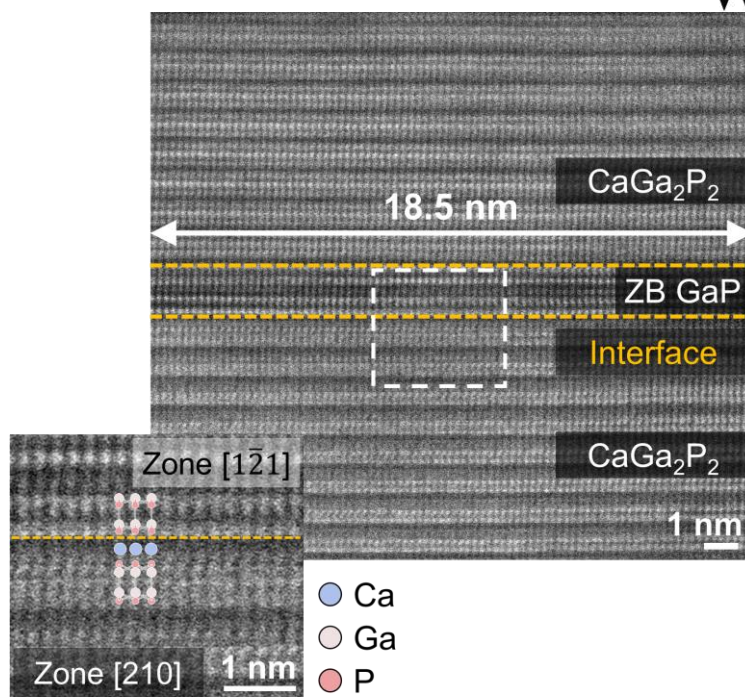


**Figure S3.** Lateral extent of the atomically sharp  $\text{CaGa}_2\text{P}_2/\text{ZB GaP}$  interface. The continuous coherent segment of the interface measured along the interface plane is 18.5 nm. The white box indicates the region corresponding to the magnified image.

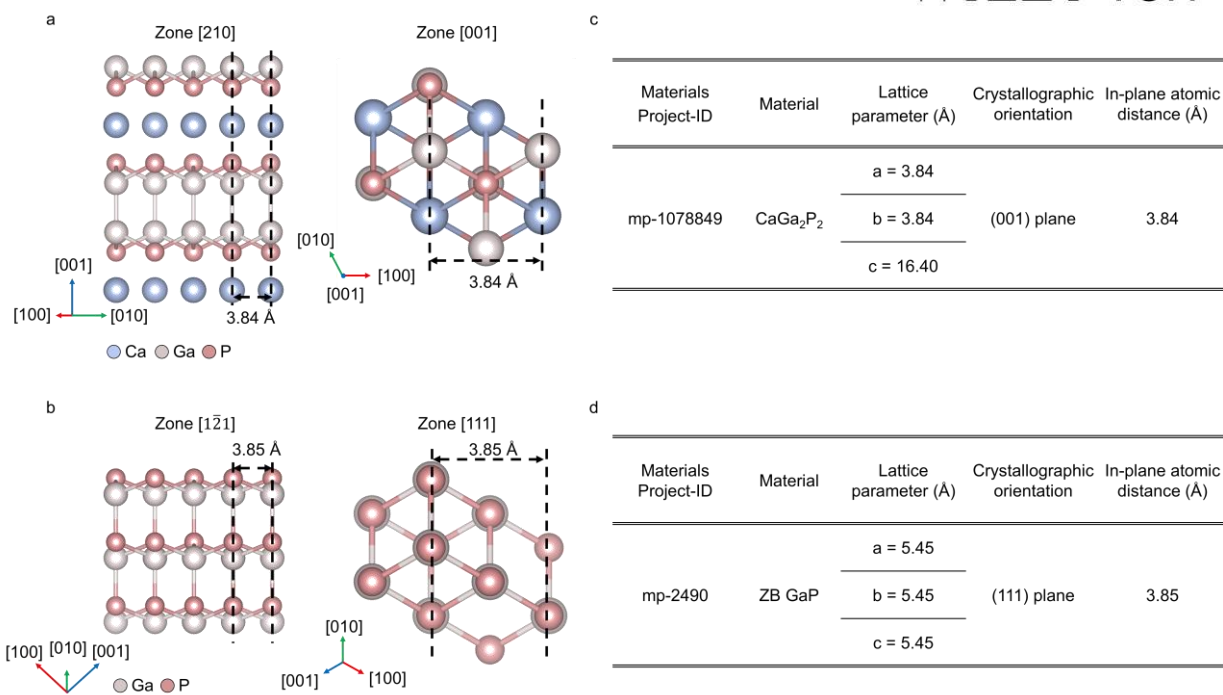


**Figure S4.** Crystallographic models used to evaluate lattice misfit between CaGa<sub>2</sub>P<sub>2</sub> (001) plane and ZB GaP (111) plane. (a) cation-eutaxy CaGa<sub>2</sub>P<sub>2</sub>. Side-view model projected along the [210] zone axis (left) and top-view projection along [001] (right). (b) ZB GaP. Side-view model projected along the [1 $\bar{2}$ 1] zone axis (left) and top-view projection along [111] (right). The misfit between the CaGa<sub>2</sub>P<sub>2</sub> (001) plane and the ZB GaP (111) plane was calculated to be 0.26%. (c,d) Tables summarizing the Materials Project IDs, lattice parameters, crystallographic orientations, and in-plane atomic distances for CaGa<sub>2</sub>P<sub>2</sub> (c) and ZB GaP (d) used for misfit calculation.

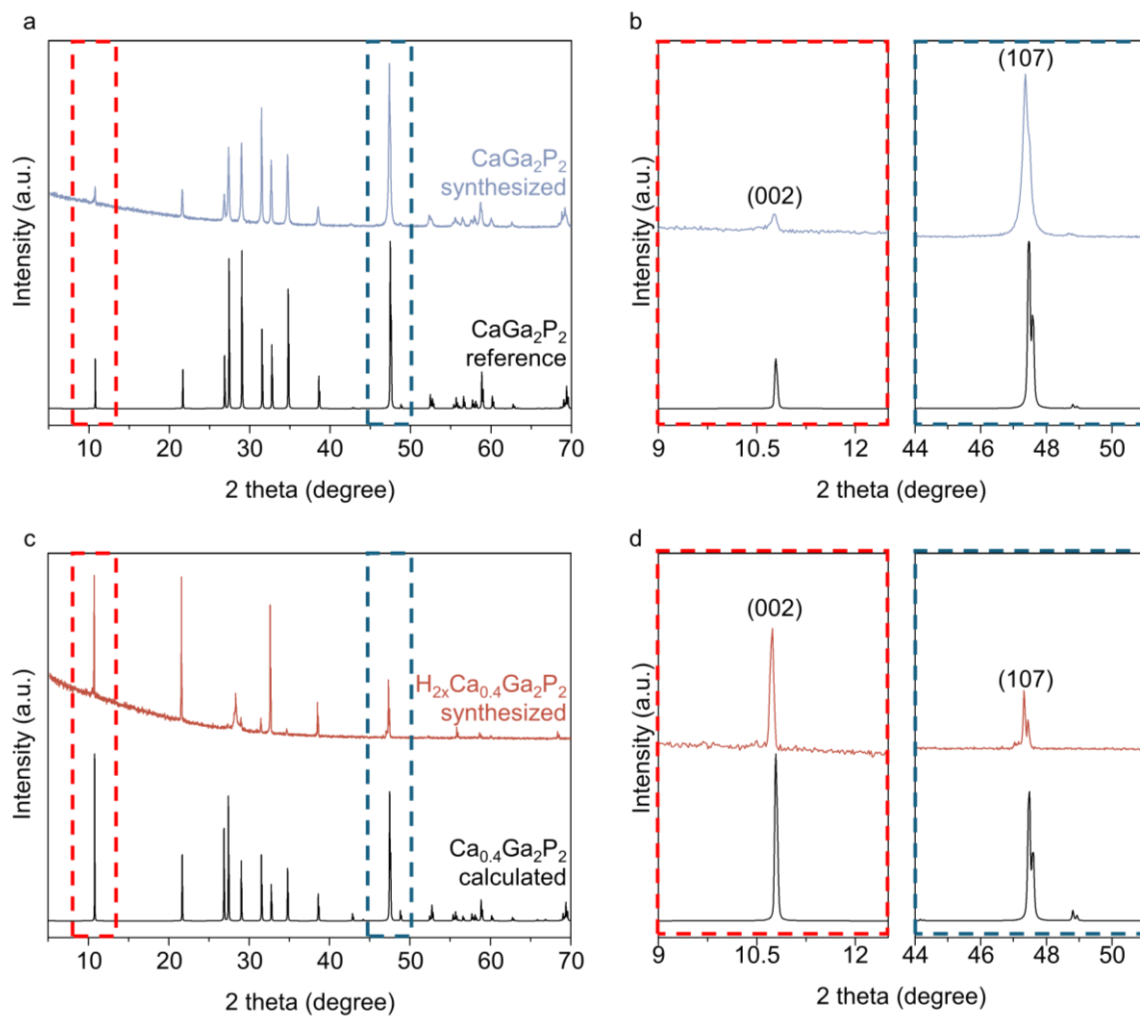


**Figure S5.** XRD patterns of  $\text{CaGa}_2\text{P}_2$  and  $\text{H}_{2x}\text{Ca}_{0.4}\text{Ga}_2\text{P}_2$ . (a) Full XRD patterns of pristine  $\text{CaGa}_2\text{P}_2$ . (b) Enlarged view of the (002) and (107) reflections in  $\text{CaGa}_2\text{P}_2$ , highlighting their intensity ratio. (c) Full XRD patterns of  $\text{H}_{2x}\text{Ca}_{0.4}\text{Ga}_2\text{P}_2$ . (d) Enlarged view of the (002) and (107) reflections in  $\text{H}_{2x}\text{Ca}_{0.4}\text{Ga}_2\text{P}_2$ , showing the Ca-content-dependent change in relative peak intensity.

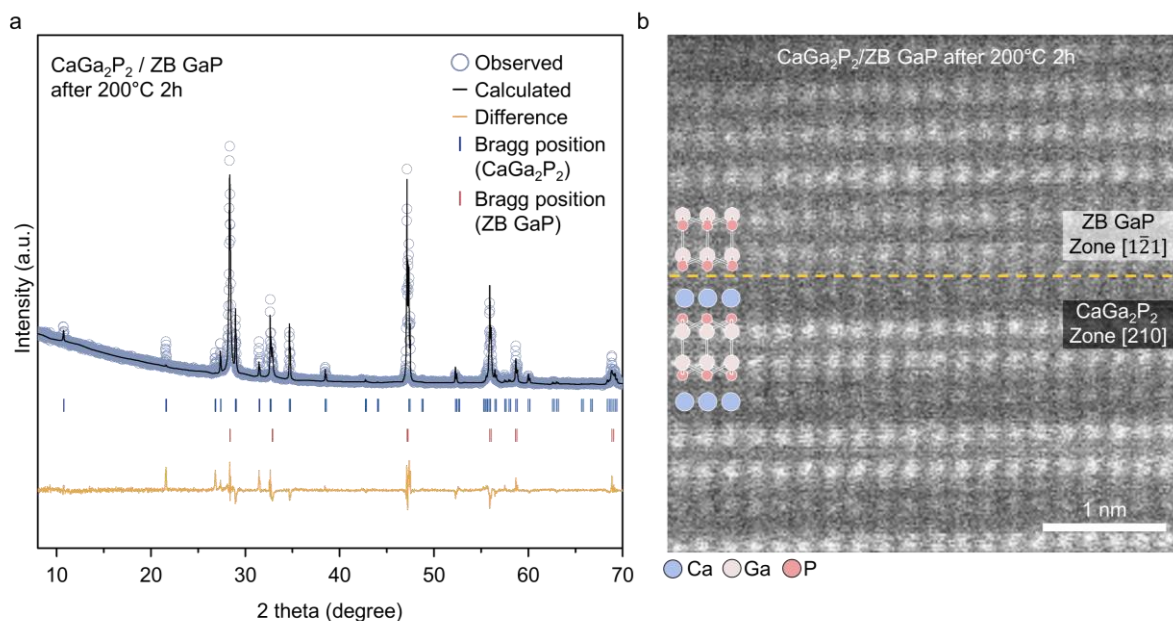


**Figure S6.** Thermal stability of the  $\text{CaGa}_2\text{P}_2/\text{ZB GaP}$  heterophase after annealing. (a) Rietveld-refined XRD patterns of the sample annealed at 200 °C for 2 h. (b) HAADF-STEM image obtained after annealing at 200 °C for 2 h. The image reveals an atomically sharp  $\text{CaGa}_2\text{P}_2/\text{ZB GaP}$  interface (yellow dashed line). In this system, migration of Ca across the heterophase interface could in principle disrupt the atomically sharp interface. However, under the present annealing conditions the interface remains intact, which is likely due to the limited out-of-plane ionic diffusion through the covalently bonded III-V framework.

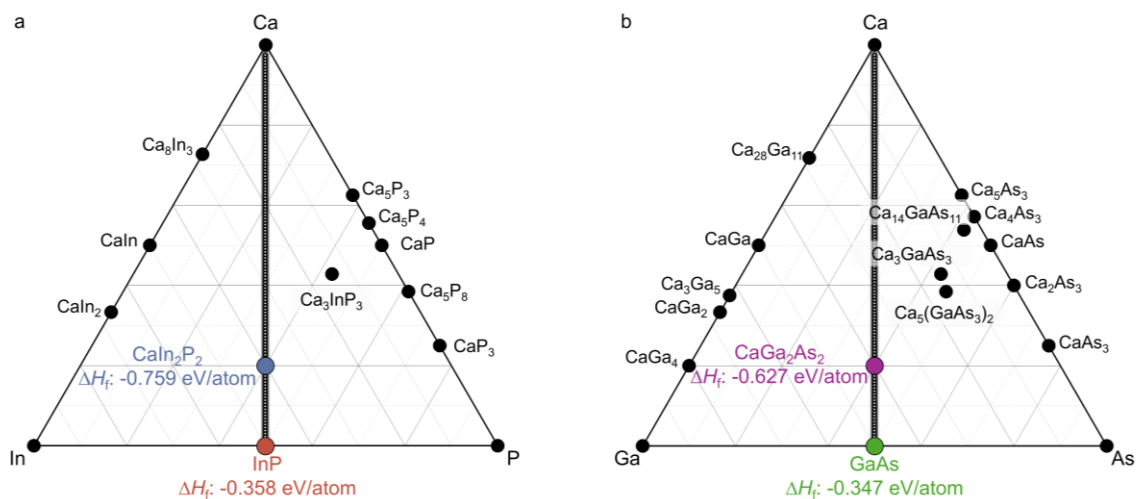


**Figure S7.** Zero-kelvin phase diagrams of cation eutaxy A–III–V systems. (a) Calculated Ca–In–P phase diagram showing  $\text{CaIn}_2\text{P}_2$  and ZB  $\text{InP}$  as the only stable end-member phases along the  $\text{Ca}_{1-x}\text{In}_2\text{P}_2$  composition line. (b) Calculated Ca–Ga–As phase diagram showing  $\text{CaGa}_2\text{As}_2$  and ZB  $\text{GaAs}$  as the only stable end-member phases along the  $\text{Ca}_{1-x}\text{Ga}_2\text{As}_2$  composition line.

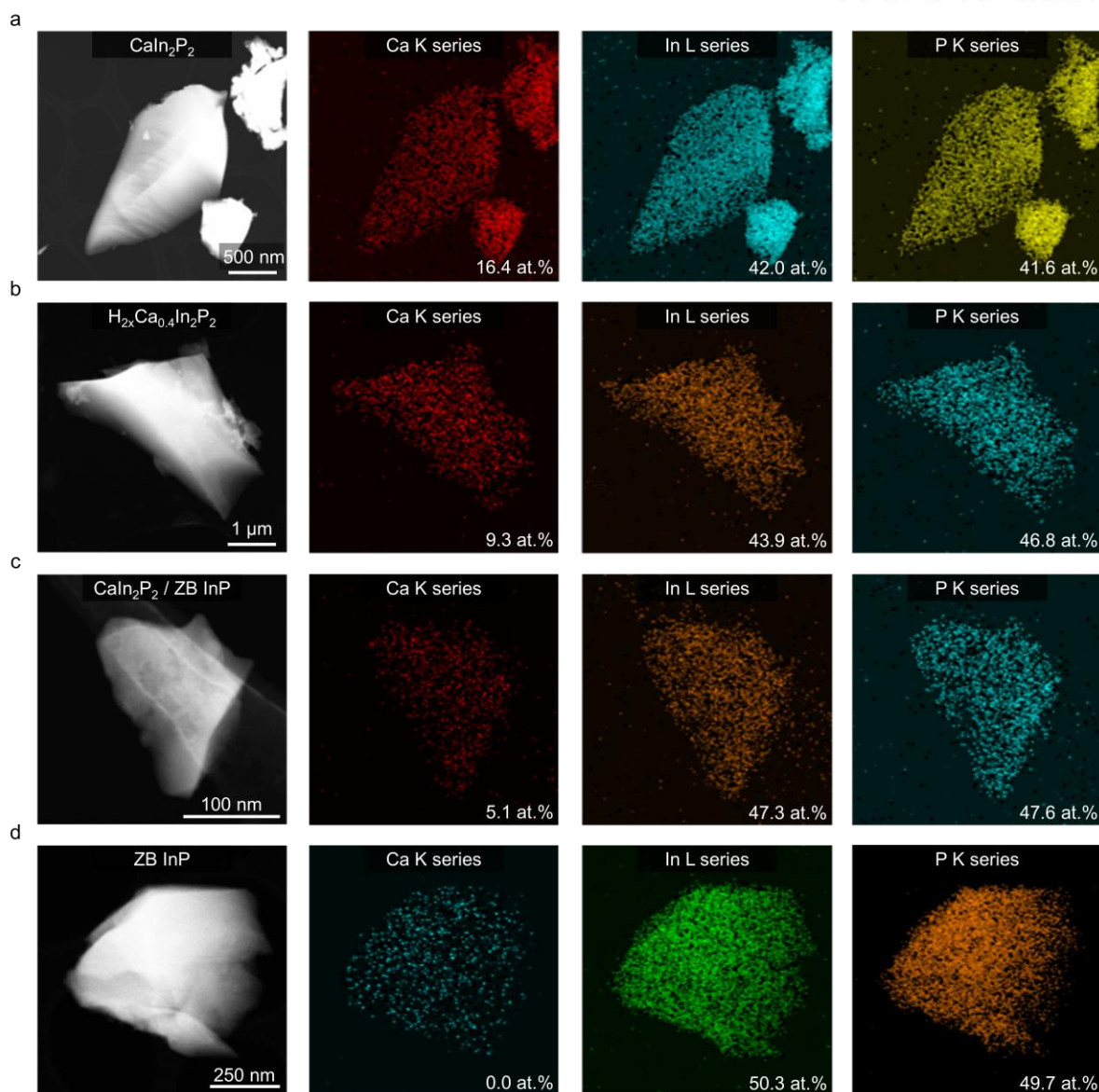


**Figure S8.** TEM–EDS elemental mapping of  $\text{CaIn}_2\text{P}_2$  specimens with different Ca contents. (a) Pristine  $\text{CaIn}_2\text{P}_2$ , showing a homogeneous distribution of all elements, with compositions of approximately Ca 16.4 at.%, In 42.0 at.%, and P 41.6 at.%. (b)  $\text{H}_{2x}\text{Ca}_{0.4}\text{In}_2\text{P}_2$ , exhibiting reduced Ca occupancy and compositions of Ca 9.3 at.%, In 43.9 at.%, and P 46.8 at.%. (c)  $\text{CaIn}_2\text{P}_2/\text{ZB InP}$ , showing further Ca depletion, with compositions Ca 5.1 at.%, In 47.3 at.%, and P 47.6 at.%. (d) Fully Ca removed ZB InP, where the In–P matrix displays compositions of In 50.3 at.% and P 49.7 at.%.

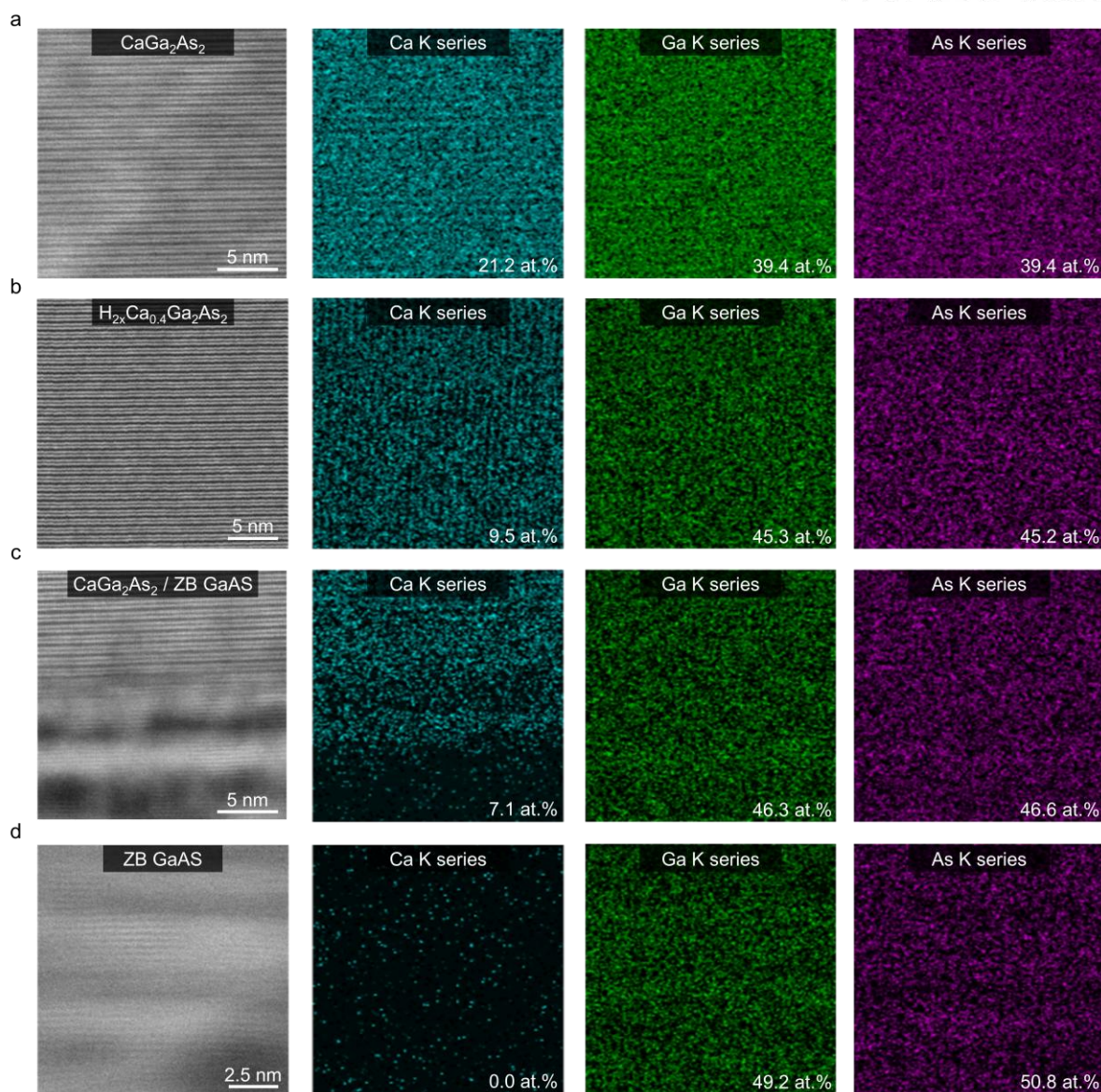


**Figure S9.** TEM-EDS elemental mapping of  $\text{CaGa}_2\text{As}_2$  specimens with different Ca contents. (a) Pristine  $\text{CaGa}_2\text{As}_2$ , showing a homogeneous elemental distribution with compositions of approximately Ca 21.2 at.%, Ga 39.4 at.%, and As 39.4 at.%. (b)  $\text{H}_{2x}\text{Ca}_{0.4}\text{Ga}_2\text{As}_2$ , exhibiting reduced Ca occupancy, with compositions Ca 9.5 at.%, Ga 45.3 at.%, and As 45.2 at.%. (c)  $\text{CaGa}_2\text{As}_2/\text{ZB GaAs}$ , showing further Ca depletion and compositions Ca 7.1 at.%, Ga 46.3 at.%, and As 46.6 at.%. (d) Fully Ca-removed ZB GaAs, where the Ga–As matrix displays compositions of Ga 49.2 at.% and As 50.8 at.%.

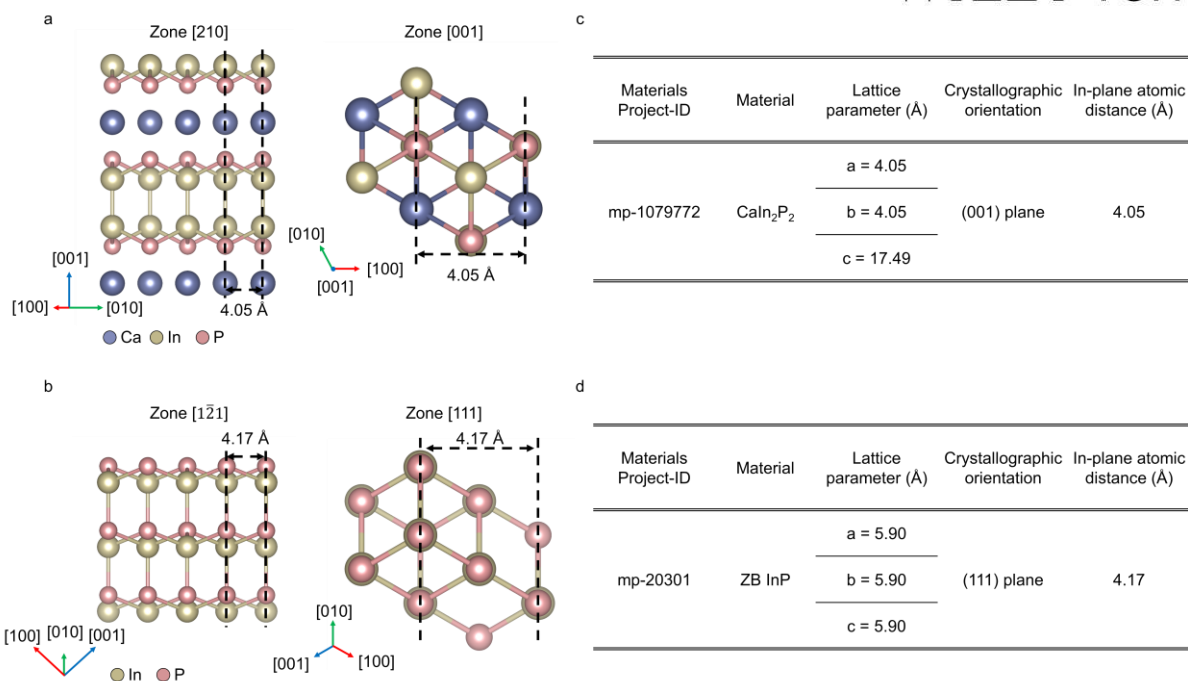


**Figure S10.** Crystallographic models used to evaluate lattice misfit between CaIn<sub>2</sub>P<sub>2</sub> (001) plane and ZB InP (111) plane. (a) cation-eutaxy CaIn<sub>2</sub>P<sub>2</sub>. Side-view model projected along the [210] zone axis (left) and top-view projection along [001] (right). (b) ZB InP. Side-view model projected along the [1 $\bar{2}$ 1] zone axis (left) and top-view projection along [111] (right). The misfit between the CaIn<sub>2</sub>P<sub>2</sub> (001) plane and the ZB InP (111) plane was calculated to be 2.96%. (c,d) Tables summarizing the Materials Project IDs, lattice parameters, crystallographic orientations, and in-plane atomic distances for CaIn<sub>2</sub>P<sub>2</sub> (c) and ZB InP (d) used for misfit calculation.

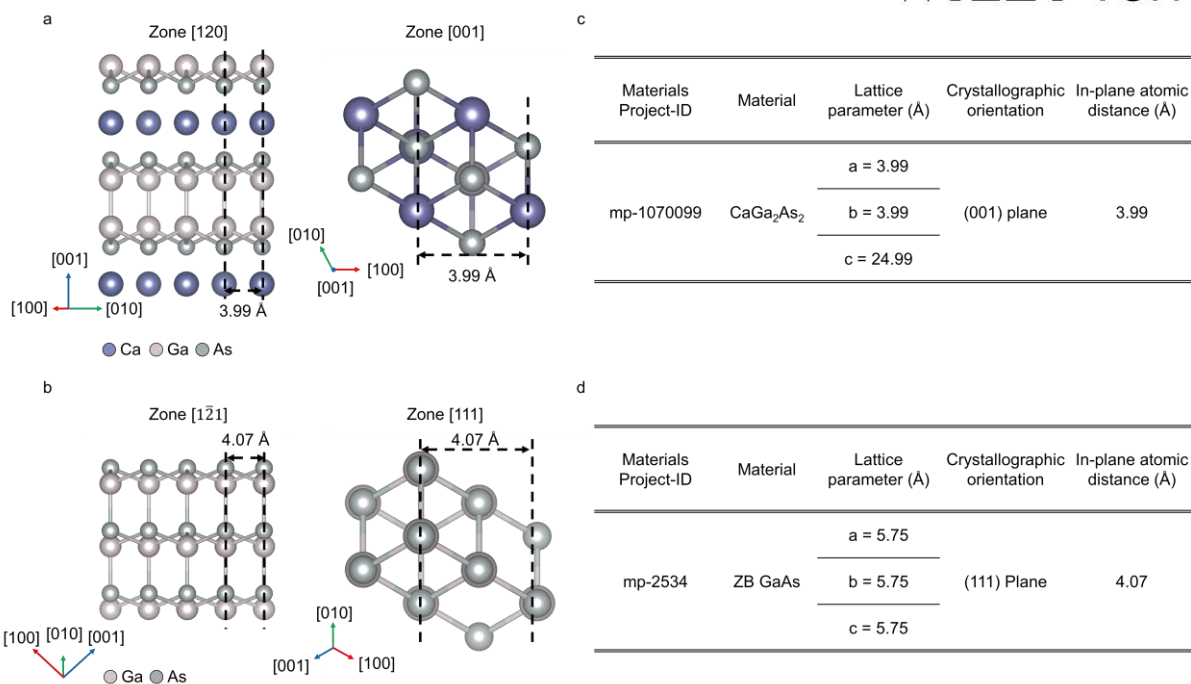


**Figure S11.** Crystallographic models used to evaluate lattice misfit between CaGa<sub>2</sub>As<sub>2</sub> (001) plane and ZB GaAs (111) plane. (a) cation-eutaxy CaGa<sub>2</sub>As<sub>2</sub>. Side-view model projected along the [120] zone axis (left) and top-view projection along [001] (right). (b) ZB GaAs. Side-view model projected along the [121] zone axis (left) and top-view projection along [111] (right). The misfit between the CaGa<sub>2</sub>As<sub>2</sub> (001) plane and the ZB GaAs (111) plane was calculated to be 2.01%. (c,d) Tables summarizing the Materials Project IDs, lattice parameters, crystallographic orientations, and in-plane atomic distances for CaGa<sub>2</sub>As<sub>2</sub> (c) and ZB GaAs (d) used for misfit calculation.

Space group:  $P6_3/mmc$  $a = 3.8375 (3) \text{ \AA}$ ,  $c = 16.4441 (18) \text{ \AA}$ ,  $V = 209.72 (3) \text{ \AA}^3$  $R_p: 7.443 \%$ ,  $R_{wp}: 11.198 \%$ ,  $R_{exp}: 5.123 \%$ ,  $R_{bragg}: 16.719 \%$ ,  $\chi^2: 4.78$ 

atom	Occ	x	y	z	$U_{iso}/U_{eq}$
Ca	1.000	0.00000	0.00000	0.00000	0.304 (5)
Ga	1.000	0.33333	0.66667	0.32354 (15)	0.0357 (17)
P	1.000	0.33333	0.66667	0.8897 (3)	0.0097 (18)

**Table S1.** Rietveld refinement and refined crystallographic parameters of pristine  $\text{CaGa}_2\text{P}_2$ .

Space group:  $P6_3/mmc$   
 $a = 3.8357 (4) \text{ \AA}$ ,  $c = 16.4599 (19) \text{ \AA}$ ,  $V = 209.73 (4) \text{ \AA}^3$   
 $R_p: 6.252 \%$ ,  $R_{wp}: 11.440 \%$ ,  $R_{exp}: 5.877 \%$ ,  $R_{bragg}: 24.861 \%$ ,  $\chi^2: 4.01$

atom	Occ	x	y	z	$U_{iso}/U_{eq}$
Ca	0.400	0.00000	0.00000	0.00000	0.07 (2)
Ga	1.000	0.33333	0.66667	0.3244 (4)	0.064 (8)
P	1.000	0.33333	0.66667	0.8952 (10)	0.039 (9)

**Table S2.** Rietveld refinement and refined crystallographic parameters of metastable cation-eutaxy single-phase  $H_{2x}Ca_{0.4}Ga_2P_2$ .

Space group:  $P6_3/mmc$  $a = 3.83881 (17) \text{ \AA}$ ,  $c = 16.4464 (8) \text{ \AA}$ ,  $V = 209.89 (2) \text{ \AA}^3$  $R_p$ : 8.919 %,  $R_{wp}$ : 12.927 %,  $R_{exp}$ : 14.831 %,  $R_{bragg}$ : 36.153 %,  $\chi^2$ : 0.76

atom	Occ	x	y	z	$U_{iso}/U_{eq}$
Ca	1.000	0.00000	0.00000	0.00000	0.00022
Ga	1.000	0.33333	0.66667	0.3227 (2)	0.00022
P	1.000	0.33333	0.66667	0.8857 (5)	0.00022

Space group:  $F\bar{4}3m$  $a = 5.449 (2) \text{ \AA}$ ,  $V = 161.79 \text{ \AA}^3$  $R_p$ : 8.919 %,  $R_{wp}$ : 12.927 %,  $R_{exp}$ : 14.831 %,  $R_{bragg}$ : 36.153 %,  $\chi^2$ : 0.76

atom	Occ	x	y	z	$U_{iso}/U_{eq}$
Ga	1.000	0.00000 (1)	0.00000 (1)	0.00000 (1)	0.06436
P	1.000	0.25000 (1)	0.25000 (1)	0.25000 (1)	0.06436

**Table S3.** Rietveld refinement results for  $\text{CaGa}_2\text{P}_2/\text{ZB GaP}$  heterophase with phase weight fractions. Rietveld refinement results confirm that  $\text{CaGa}_2\text{P}_2$  has a weight fraction of 17% and ZB GaP has a fraction of 83%.

Space group:  $P6_3/mmc$  $a = 3.8370 (3) \text{ \AA}$ ,  $c = 16.4485 (15) \text{ \AA}$ ,  $V = 209.72 (3) \text{ \AA}^3$  $R_p$ : 6.37 %,  $R_{wp}$ : 9.49 %,  $R_{exp}$ : 4.65 %,  $R_{bragg}$ : 7.97 %,  $\chi^2$ : 4.17

atom	Occ	x	y	z	$U_{iso}/U_{eq}$
Ca	1.000	0.00000	0.00000	0.00000	0.02
Ga	1.000	0.33333	0.66667	0.3257 (5)	0.02
P	1.000	0.33333	0.66667	0.8884 (10)	0.02

Space group:  $F\bar{4}3m$  $a = 5.449 (3) \text{ \AA}$ ,  $V = 161.82 \text{ \AA}^3$  $R_p$ : 6.37 %,  $R_{wp}$ : 9.49 %,  $R_{exp}$ : 4.65 %,  $R_{bragg}$ : 7.97 %,  $\chi^2$ : 4.17

atom	Occ	x	y	z	$U_{iso}/U_{eq}$
Ga	1.000	0.00000 (1)	0.00000 (1)	0.00000 (1)	0.03
P	1.000	0.25000 (1)	0.25000 (1)	0.25000 (1)	0.03

**Table S4.** Rietveld refinement results for the  $\text{CaGa}_2\text{P}_2/\text{ZB GaP}$  heterophase after annealing at 200 °C for 2 h. The refinement confirms that the weight fractions of the phases are 25.2%  $\text{CaGa}_2\text{P}_2$  and 74.8% ZB GaP.

Space group:  $F\bar{4}3m$   
 $a = 5.441(2) \text{ \AA}$ ,  $V = 161.11 \text{ \AA}^3$   
 $R_p$ : 9.393 %,  $R_{wp}$ : 14.406 %,  $R_{exp}$ : 16.269 %,  $R_{bragg}$ : 21.797 %,  $\chi^2$ : 0.784

atom	Occ	x	y	z	$U_{iso}/U_{eq}$
Ga	1.000	0.00000	0.00000	0.00000	0.04179
P	1.000	0.25000	0.25000	0.25000	0.02732

**Table S5.** Rietveld refinement and refined crystallographic parameters of ZB GaP.

**Supplementary Notes****Note S1.** Misfit-dislocation–limited lateral extent of atomically sharp interfaces

In this study, an atomically sharp interface refers to a boundary across which atomic column registry is preserved between the two phases. Within this definition, the lateral distance over which such coherent registry can be maintained is primarily limited by the formation of misfit dislocations. When misfit dislocations are present, coherent alignment of the interface can be disrupted by the dislocation cores, where local lattice distortion prevents ideal atomic registry.

The spacing ( $D$ ) between misfit dislocations can be approximated as

$$D \approx \frac{a_{film}}{f}$$

where  $a_{film}$  is the in-plane lattice periodicity of the film and  $f$  is the lattice misfit.

For the  $\text{CaGa}_2\text{P}_2/\text{ZB GaP}$  interface, the calculated lattice misfit is  $f = 0.0026$ . Using the in-plane lattice periodicity of ZB GaP ( $a_{film} = 3.85 \text{ \AA}$ ), the estimated dislocation spacing is  $D \approx 148 \text{ nm}$ . This estimate suggests that the atomically sharp interface could extend laterally up to  $\sim 148 \text{ nm}$  before the introduction of misfit dislocations.

In HAADF–STEM measurements, atomic-resolution information can typically be reliably tracked over lateral distances of several tens of nanometers. Within this observation window, the  $\text{CaGa}_2\text{P}_2/\text{ZB GaP}$  interface remains atomically coherent, and continuous atomic-column registry is observed over a lateral distance of approximately  $18 \text{ nm}$  (Figure S3).

**Note S2.** Analysis of interface stability through comparison of misfit-dependent strain energy density

To understand why the atomically sharp interface observed in the CaGa<sub>2</sub>P<sub>2</sub>/ZB GaP heterophase forms and remains stable, we analyzed the relationship between the interface energy ( $\gamma_{\text{interface}}$ ) and the lattice misfit ( $f$ ). In general, a lower  $\gamma_{\text{interface}}$  suppresses interfacial roughening, interdiffusion, and defect accumulation, thereby favoring the preservation of continuous atomic registry and the stability of atomically sharp interfaces. The interface energy can be decomposed into chemical and structural contributions:

$$\gamma_{\text{interface}} = \gamma_{\text{bond}} + \gamma_{\text{structure}}$$

where  $\gamma_{\text{bond}}$  represents the contribution from chemical bonding across the interface and  $\gamma_{\text{structure}}$  arises from structural effects associated with lattice matching. For coherent interfaces,  $\gamma_{\text{structure}}$  can be approximated as the elastic strain energy term ( $\gamma_{\text{strain}}$ ). Within the first-order approximation of linear elasticity, the strain energy scales with the square of the lattice misfit:

$$\gamma_{\text{strain}} \propto E f^2$$

where  $E$  is the effective elastic modulus and  $f = (a_{\text{film}} - a_{\text{substrate}})/a_{\text{substrate}}$  is the lattice misfit defined by the in-plane lattice parameters of the two phases.

The CaGa<sub>2</sub>P<sub>2</sub> (001)/ZB GaP (111) interface observed in this work maintains atomically coherent registry and exhibits an exceptionally small misfit (~0.26%). This makes the system suitable for evaluating the relative elastic penalty associated with lattice mismatch. To place this value in context, we calculated  $f$  for 14 additional candidate interfaces constructed from combinations of low-index planes between the two phases.

The CaGa<sub>2</sub>P<sub>2</sub> (001)/ZB GaP (111) interface uniquely satisfies periodic atomic registry at the primitive surface unit-cell (1×1) level, yielding a misfit of 0.26% (Figure S4). In contrast,

other low-index plane combinations do not share a common translational periodicity at the  $1\times 1$  level because their surface lattice vectors differ in length, angle, and symmetry. For these cases, commensurate supercells were constructed using integer multiples of the two surface lattices to establish periodic atomic registry, and the effective in-plane lattice parameters of the supercells were used to calculate the misfit. The resulting misfits for these candidate interfaces range from 0.91% to 2.72% (Figure S12a–o).

We then compared the relative elastic penalties using the scaling relation  $\gamma_{\text{strain}} \propto E t^2$ . A rigorous evaluation of the absolute strain energy per unit area requires knowledge of the effective strained thickness ( $t_{\text{eff}}$ ). However,  $t_{\text{eff}}$  cannot be uniquely defined for hypothetical interfaces composed of different plane combinations. Therefore, we compared the strain energy density, which does not depend on  $t_{\text{eff}}$ , to evaluate the relative elastic penalty among the candidate interfaces. This analysis shows that the strain energy density of the alternative low-index interfaces is approximately 12–125 times larger than that of the  $\text{CaGa}_2\text{P}_2$  (001)/ZB GaP (111) interface (Figure S12p).

All candidate interfaces considered here involve the same  $\text{CaGa}_2\text{P}_2$ /ZB GaP phase combination, and the elemental species participating in interfacial bonding are therefore identical. Variations in the chemical bonding contribution ( $\gamma_{\text{bond}}$ ) are thus expected to be limited. Consequently, differences in  $\gamma_{\text{interface}}$  are primarily governed by the misfit-dependent strain term  $\gamma_{\text{strain}}$ . These results indicate that the  $\text{CaGa}_2\text{P}_2$  (001)/ZB GaP (111) interface, which has the smallest lattice misfit, also has the lowest elastic penalty and therefore represents the most energetically favorable interface configuration. This interpretation is consistent with the experimental observation that this interface forms and remains atomically sharp.

A similar trend was also observed in the  $\text{CaIn}_2\text{P}_2$ /ZB InP (Figure S13) and  $\text{CaGa}_2\text{As}_2$ /ZB GaAs (Figure S14) systems.



ZB GaP	CaGa <sub>2</sub> P <sub>2</sub>	Misfit (%)	ZB GaP	CaGa <sub>2</sub> P <sub>2</sub>	Misfit (%)
	(001)	1.65	(001)	(001)	1.65
	(110)	1.37	(110)	(110)	2.72
(001)	(100)	1.38	(110)	(100)	2.72
	(111)	1.65	(111)	(111)	1.32
	(011)	1.38	(011)	(011)	0.91

ZB GaP	CaGa <sub>2</sub> P <sub>2</sub>	Misfit (%)
	(110)	1.83
(111)	(100)	1.83
	(111)	1.32
	(011)	0.91

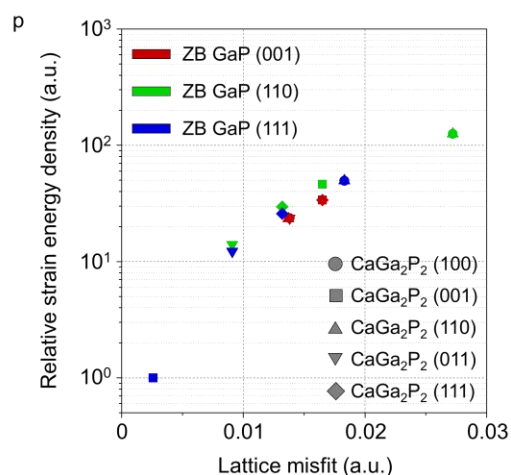


**Figure S12.** Lattice matching analysis and misfit-dependent elastic penalty comparison for  $\text{CaGa}_2\text{P}_2/\text{ZB GaP}$  interfaces constructed from low-index planes. Minimum matching surface supercells were constructed to define periodic interface models with a common in-plane translational periodicity for different combinations of low-index planes. The supercell multipliers used for each interface are as follows: (a) ZB GaP (001),  $6 \times 5$  supercell;  $\text{CaGa}_2\text{P}_2$  (001),  $5 \times 7$  supercell. (b) ZB GaP (001),  $10 \times 3$  supercell;  $\text{CaGa}_2\text{P}_2$  (110),  $7 \times 2$  supercell. (c) ZB GaP (001),  $5 \times 3$  supercell;  $\text{CaGa}_2\text{P}_2$  (100),  $7 \times 2$  supercell. (d) ZB GaP (001),  $6 \times 6$  supercell;  $\text{CaGa}_2\text{P}_2$  (111),  $5 \times 1$  supercell. (e) ZB GaP (001),  $5 \times 6$  supercell;  $\text{CaGa}_2\text{P}_2$  (011),  $7 \times 1$  supercell. (f) ZB GaP (110),  $6 \times 1$  supercell;  $\text{CaGa}_2\text{P}_2$  (001),  $5 \times 1$  supercell. (g) ZB GaP (110),  $17 \times 2$  supercell;  $\text{CaGa}_2\text{P}_2$  (110),  $11 \times 1$  supercell. (h) ZB GaP (110),  $17 \times 1$  supercell;  $\text{CaGa}_2\text{P}_2$  (100),  $11 \times 1$  supercell. (i) ZB GaP (110),  $7 \times 6$  supercell;  $\text{CaGa}_2\text{P}_2$  (111),  $4 \times 1$  supercell. (j) ZB GaP (110),  $6 \times 1$  supercell;  $\text{CaGa}_2\text{P}_2$  (011),  $1 \times 1$  supercell. (k) ZB GaP (111),  $5 \times 2$  supercell;  $\text{CaGa}_2\text{P}_2$  (110),  $4 \times 1$  supercell. (l) ZB GaP (111),  $5 \times 1$  supercell;  $\text{CaGa}_2\text{P}_2$  (100),  $4 \times 1$  supercell. (m) ZB GaP (111),  $7 \times 5$  supercell;  $\text{CaGa}_2\text{P}_2$  (111),  $4 \times 1$  supercell. (n) ZB GaP (111),  $5 \times 1$  supercell;  $\text{CaGa}_2\text{P}_2$  (011),  $1 \times 1$  supercell. (o) Summary of the lattice misfit values calculated based on the matched in-plane periodicity. (p) Relative elastic strain energy density estimated from the calculated misfit values and the elastic modulus of ZB GaP corresponding to the exposed crystallographic plane. The strain energy density is normalized to that of the  $\text{CaGa}_2\text{P}_2$  (001)/ZB GaP (111) interface, whose misfit value is taken from Figure S4.

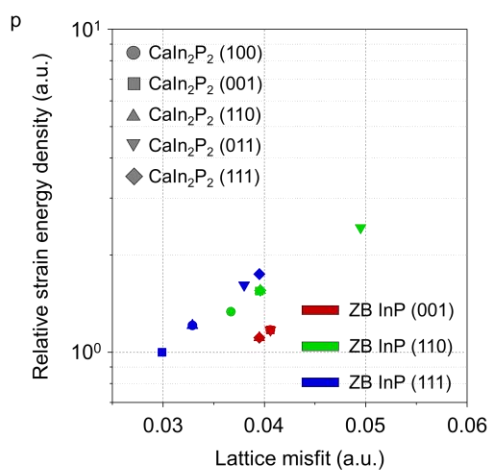


**o**

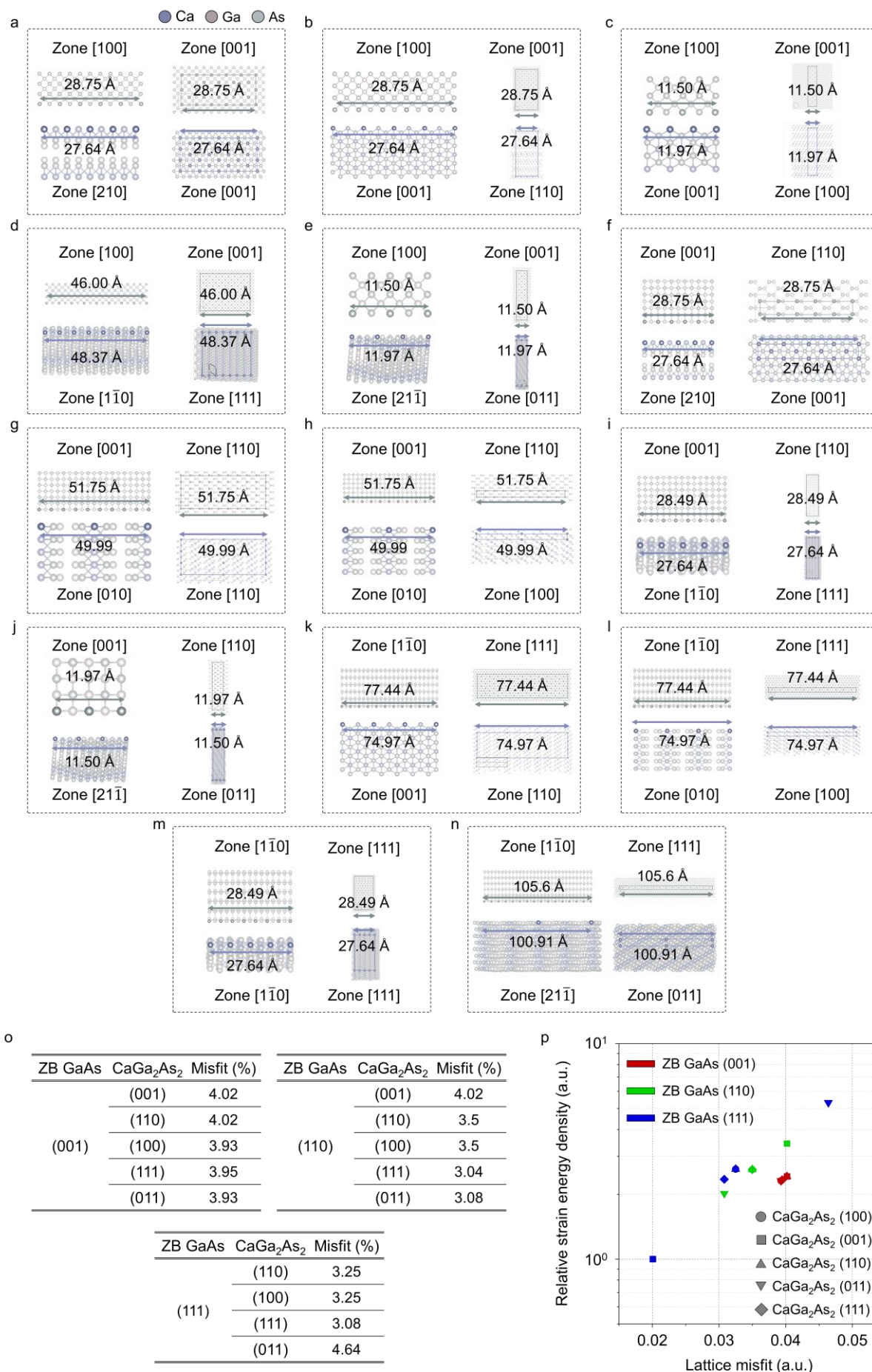
ZB InP	CaIn <sub>2</sub> P <sub>2</sub>	Misfit (%)	ZB InP	CaIn <sub>2</sub> P <sub>2</sub>	Misfit (%)
	(001)	4.06		(001)	3.95
	(110)	3.95		(110)	3.96
(001)	(100)	4.06	(110)	(100)	3.67
	(111)	3.95		(111)	3.96
	(011)	4.06		(011)	4.95

ZB InP	CaIn <sub>2</sub> P <sub>2</sub>	Misfit (%)
	(110)	3.29
(111)	(100)	3.29
	(111)	3.95
	(011)	3.8



**Figure S13.** Lattice matching analysis and misfit-dependent elastic penalty comparison for  $\text{CaIn}_2\text{P}_2/\text{ZB InP}$  interfaces constructed from low-index planes. Minimum matching surface supercells were constructed to define periodic interface models with a common in-plane translational periodicity for different combinations of low-index planes. The supercell multipliers used for each interface are as follows: (a) ZB InP (001),  $5 \times 6$  supercell;  $\text{CaIn}_2\text{P}_2$  (001),  $7 \times 5$  supercell. (b) ZB InP (001),  $8 \times 3$  supercell;  $\text{CaIn}_2\text{P}_2$  (110),  $7 \times 2$  supercell. (c) ZB InP (001),  $5 \times 3$  supercell;  $\text{CaIn}_2\text{P}_2$  (100),  $7 \times 2$  supercell. (d) ZB InP (001),  $8 \times 6$  supercell;  $\text{CaIn}_2\text{P}_2$  (111),  $7 \times 1$  supercell. (e) ZB InP (001),  $5 \times 6$  supercell;  $\text{CaIn}_2\text{P}_2$  (011),  $7 \times 1$  supercell. (f) ZB InP (110),  $8 \times 7$  supercell;  $\text{CaIn}_2\text{P}_2$  (001),  $7 \times 1$  supercell. (g) ZB InP (110),  $7 \times 3$  supercell;  $\text{CaIn}_2\text{P}_2$  (110),  $4 \times 2$  supercell. (h) ZB InP (110),  $10 \times 1$  supercell;  $\text{CaIn}_2\text{P}_2$  (100),  $7 \times 1$  supercell. (i) ZB InP (110),  $7 \times 6$  supercell;  $\text{CaIn}_2\text{P}_2$  (111),  $4 \times 1$  supercell. (j) ZB InP (110),  $9 \times 8$  supercell;  $\text{CaIn}_2\text{P}_2$  (011),  $1 \times 7$  supercell. (k) ZB InP (111),  $5 \times 5$  supercell;  $\text{CaIn}_2\text{P}_2$  (110),  $4 \times 3$  supercell. (l) ZB InP (111),  $5 \times 1$  supercell;  $\text{CaIn}_2\text{P}_2$  (100),  $4 \times 1$  supercell. (m) ZB InP (111),  $7 \times 5$  supercell;  $\text{CaIn}_2\text{P}_2$  (111),  $4 \times 1$  supercell. (n) ZB InP (111),  $19 \times 1$  supercell;  $\text{CaIn}_2\text{P}_2$  (011),  $4 \times 1$  supercell. (o) Summary of the lattice misfit values calculated based on the matched in-plane periodicity. (p) Relative elastic strain energy density estimated from the calculated misfit values and the elastic modulus of ZB InP corresponding to the exposed crystallographic plane. The strain energy density is normalized to that of the  $\text{CaIn}_2\text{P}_2$  (001)/ZB InP (111) interface, whose misfit value is taken from Figure S10.



**Figure S14.** Lattice matching analysis and misfit-dependent elastic penalty comparison for  $\text{CaGa}_2\text{As}_2/\text{ZB GaAs}$  interfaces constructed from low-index planes. Minimum matching surface supercells were constructed to define periodic interface models with a common in-plane translational periodicity for different combinations of low-index planes. The supercell multipliers used for each interface are as follows: (a) ZB GaAs (001),  $5 \times 2$  supercell;  $\text{CaGa}_2\text{As}_2$  (001),  $4 \times 3$  supercell. (b) ZB GaAs (001),  $5 \times 9$  supercell;  $\text{CaGa}_2\text{As}_2$  (110),  $4 \times 2$  supercell. (c) ZB GaAs (001),  $2 \times 9$  supercell;  $\text{CaGa}_2\text{As}_2$  (100),  $3 \times 2$  supercell. (d) ZB GaAs (001),  $8 \times 6$  supercell;  $\text{CaGa}_2\text{As}_2$  (111),  $7 \times 1$  supercell. (e) ZB GaAs (001),  $2 \times 9$  supercell;  $\text{CaGa}_2\text{As}_2$  (011),  $3 \times 1$  supercell. (f) ZB GaAs (110),  $5 \times 1$  supercell;  $\text{CaGa}_2\text{As}_2$  (001),  $4 \times 1$  supercell. (g) ZB GaAs (110),  $9 \times 5$  supercell;  $\text{CaGa}_2\text{As}_2$  (110),  $2 \times 3$  supercell. (h) ZB GaAs(110),  $9 \times 1$  supercell;  $\text{CaGa}_2\text{As}_2$  (100),  $2 \times 1$  supercell. (i) ZB GaAs (110),  $7 \times 17$  supercell;  $\text{CaGa}_2\text{As}_2$  (111),  $4 \times 2$  supercell. (j) ZB GaAs (110),  $2 \times 12$  supercell;  $\text{CaGa}_2\text{As}_2$  (011),  $3 \times 1$  supercell. (k) ZB GaAs (111),  $11 \times 5$  supercell;  $\text{CaGa}_2\text{As}_2$  (110),  $3 \times 3$  supercell. (l) ZB GaAs (110),  $11 \times 1$  supercell;  $\text{CaGa}_2\text{As}_2$  (100),  $3 \times 1$  supercell. (m) ZB GaAs (111),  $7 \times 7$  supercell;  $\text{CaGa}_2\text{As}_2$  (111),  $4 \times 1$  supercell. (n) ZB GaAs (111),  $15 \times 1$  supercell;  $\text{CaGa}_2\text{As}_2$  (011),  $2 \times 1$  supercell. (o) Summary of the lattice misfit values calculated based on the matched in-plane periodicity. (p) Relative elastic strain energy density estimated from the calculated misfit values and the elastic modulus of ZB GaAs corresponding to the exposed crystallographic plane. The strain energy density is normalized to that of the  $\text{CaGa}_2\text{As}_2$  (001)/ZB GaAs (111) interface, whose misfit value is taken from Figure S11.

## Supplementary Methods

*Calculation of lattice misfit between A-III-V and III-V phases:* The lattice misfit between layered A-III-V compounds and the corresponding III-V precipitate phases was evaluated based on geometric lattice matching between the matrix and precipitate structures. In the present system, the III-V phase (e.g., GaP, GaAs, and InP) forms as a secondary precipitate within the A-III-V host crystal through selective removal of the A-site cation, rather than through external epitaxial deposition. Accordingly, following established precipitate-matrix interface models, the A-III-V phase was defined as the substrate (matrix) and the III-V phase as the film (precipitate) when evaluating the lattice misfit.

Crystallographic information files (CIFs) for all A-III-V and III-V compounds were obtained from the Materials Project database. For each crystallographic plane, the in-plane lattice periodicity was defined as the center-to-center distance between periodically repeating atomic rows within that plane.

The lattice misfit ( $f$ ) at each A-III-V/III-V interface was calculated using

$$f = \frac{a_{\text{film}} - a_{\text{substrate}}}{a_{\text{substrate}}}$$

where  $a_{\text{film}}$  and  $a_{\text{substrate}}$  represent the in-plane lattice periodicities of the III-V precipitate phase and the A-III-V matrix phase, respectively. The lattice parameters, crystallographic orientations, Materials Project IDs, and in-plane atomic distances used in the misfit calculations are summarized in the tables provided in Figures S4, S10, and S11 to ensure full reproducibility of the analysis.

For the 14 additional interfaces constructed from combinations of low-index planes, cases in which the two surface lattices were incommensurate at the  $1 \times 1$  level were treated by constructing commensurate supercells. The in-plane lattices of each surface were expanded by integer multiples to obtain a common periodicity. Supercell combinations were selected such that the residual lattice mismatch between the two surfaces was less than 5%, while keeping the supercell area minimal. The lattice misfit was then calculated using the in-plane lattice periodicity defined by the matched supercells.

## References

1. J. W. Matthews, and A. E. Blakeslee, "Defects in epitaxial multilayers: I. Misfit dislocations," *Journal of Crystal Growth* **27** (1974): 118–125, [https://doi.org/10.1016/S0022-0248\(74\)80055-2](https://doi.org/10.1016/S0022-0248(74)80055-2)
2. D. A. Porter, and K. E. Easterling, *Phase Transformations in Metals and Alloys*, 2nd ed. (Boston, MA: Springer US, 1992).
3. Y. L. Tang, Y. L. Zhu, and X. L. Ma, "On the benefit of aberration-corrected HAADF-STEM for strain determination and its application to tailoring ferroelectric domain patterns," *Ultramicroscopy* **160** (2016): 57–63, <https://doi.org/10.1016/j.ultramic.2015.09.014>
4. W. W. Mullins, "Theory of Thermal Grooving," *Journal of Applied Physics* **28** (1957): 333–339, <https://doi.org/10.1063/1.1722742>
5. M. Gonzalez-Debs, J. G. Cederberg, R. M. Biefeld, and T. F. Kuech, "Photoluminescence studies on Al and Ga interdiffusion across (Al,Ga)Sb/GaSb quantum well interfaces," *Journal of Applied Physics* **97** (2005): 103522, <https://doi.org/10.1063/1.1900286>
6. L. B. Freund, and S. Suresh, *Thin Film Materials: Stress, Defect Formation and Surface Evolution*, 1st ed. (Cambridge: Cambridge University Press, 2004), <https://doi.org/10.1017/CBO9780511754715>
7. K. H. L. Zhang, V. K. Lazarov, P. L. Galindo, et al., "Domain Matching Epitaxial Growth of In<sub>2</sub>O<sub>3</sub> Thin Films on  $\alpha$ -Al<sub>2</sub>O<sub>3</sub>(0001)," *Crystal Growth & Design* **12** (2012): 1000–1007, <https://doi.org/10.1021/cg201474h>